Quasi-Alvarez drift-tube linac structures for heavy ion therapy accelerator facilities

Mohammad Reza Khalvati[1,2,*] Vittorio Bencini[1] and Suitbert Ramberger[1,†]

[1]*European Organization for Nuclear Research (CERN), 1211 Geneva 23, Switzerland*
[2]*School of Particles and Accelerators, Institute for Research in Fundamental Sciences (IPM), P.O. Box 19395-5531, Tehran, Iran*

(Received 4 October 2021; revised 21 December 2022; accepted 6 January 2023; published 16 February 2023)

Next generation heavy ion therapy and research facilities require efficient accelerating structures. Particularly, at low beam energies, right after the standard scheme of the ion source, low-energy beam transfer, and radio-frequency quadrupole (RFQ), several options for accelerating structures are available including the classic drift-tube linac (DTL), the interdigital H-mode DTL (IH-DTL), and superconducting quarter-wave resonators. These structures need to integrate the beam acceleration with the focusing channel, nowadays typically provided by permanent-magnet quadrupoles (PMQs). The frequency of operation needs to be in line with that of the RFQ structure, and it has been chosen at 750 MHz for practical considerations for the Next Ion Medical Machine Study (NIMMS) that is the application focus of this manuscript. While classic DTL structures at low ion beam energies do not provide enough space for PMQs at that frequency within a single $\beta\lambda$ period, IH-DTL structures do not provide the regular focusing channel with consequences on the beam quality. For these reasons, quasi-Alvarez drift-tube linac (QA-DTL) structures are reevaluated in this manuscript as they might fill this gap. They have not received much attention in the literature so far and therefore their design is described in detail. The design procedure presented here may serve as a blueprint for DTL design in general. In addition to the overall rf design, axial field stabilization with a new technique and multiphysics studies of the rf structure are described. A cost estimation completes the NIMMS QA-DTL study.

DOI: 10.1103/PhysRevAccelBeams.26.022001

I. INTRODUCTION

Options for a next generation heavy ion therapy and research facility are under investigation within the Next Ion Medical Machine Study (NIMMS) initiative at CERN [1]. Deploying heavier ions like carbon in the treatment of cancerous tumors provides sharper dose distribution [2]. In addition, due to higher relative biological effectiveness compared to proton or photon irradiation, carbon irradiation is more appropriate for the treatment of radio-resistant tumors [3]. The NIMMS design aims at a treatment energy of up to 430 MeV/nucleon either with a synchrotron design delivering beams of fully stripped carbon ions with an intensity of 2×10^{10} particles per cycle, or—as an alternative—with a full-linac design delivering more than 10^9 ions per 5 μs pulse at a repetition rate of 200 Hz. The target synchrotron intensity is about 20 times higher than at current facilities such as the Heidelberg Ion Beam Therapy Center (HIT, Heidelberg, Germany) and the National Center of Oncological Hadrontherapy (CNAO, Pavia, Italy), resulting in faster treatment of patients [4,5]. The full-linac beam intensity is higher as well, and being distributed over several short pulses, can be precisely deposited on the tumor, in particular, in the longitudinal direction thanks to accurate pulse-to-pulse energy modulation.

The objective of the NIMMS initiative is to design and compare accelerator layouts that meet nominal beam requirements, as well as minimize their costs. The reference user of the NIMMS design is the new ion therapy research facility proposed for South East Europe by the South East European International Institute for Sustainable Technologies (SEEIIST) [6]. This facility will include several experimental beamlines for a wide range of research applications ranging from biomedical and nuclear physics studies to material research.

Three accelerator designs are proposed for the NIMMS facility layout: The first design option is a normal-conducting synchrotron. The layout of the synchrotron is shown in Fig. 1(a). A linac injects an 800-μA beam into the synchrotron ring. As an additional feature, the linac injector could be used to provide a 7-MeV/nucleon beam of

*Khalvati@ipm.ir
†Suitbert.Ramberger@cern.ch

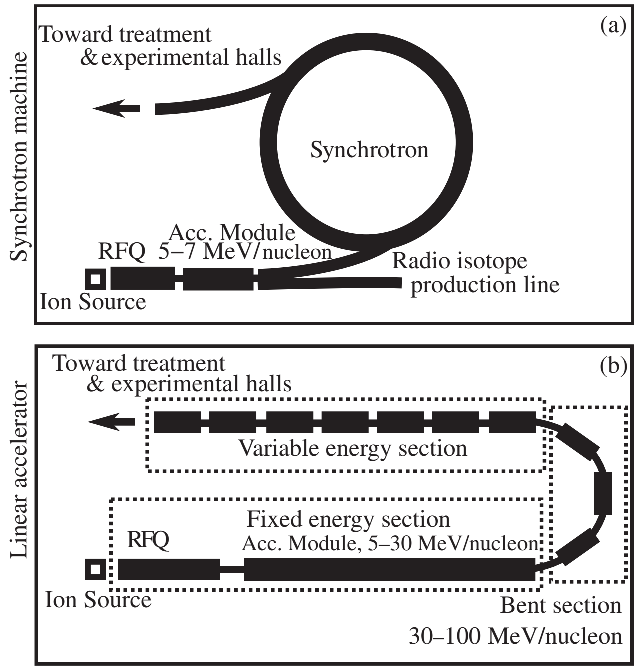

FIG. 1. (a) The NIMMS reference synchrotron layout for the NIMMS facility. (b) The full high-frequency linac design for C^{6+} acceleration [8]. Note the schematic layouts are not to scale.

α particles, having the same charge-to-mass ratio as C^{6+}, for radioisotope production [7]. The second design option is based on a superconducting synchrotron ring. While its main advantage is the comparably smaller footprint, it comes with higher complexity and expected costs. While superconducting linac technology exists, even in this scenario, a reasonable cost-effective medical facility would rather use a normal-conducting linac as an injector as described in the first design option. Finally, a full high-frequency normal-conducting linac is the third option that is under design. The layout of the NIMMS linac is shown in Fig. 1(b). The linac comprises a 30-MeV/nucleon fixed energy section and a variable energy section covering the range between 100 and 430 MeV/nucleon. The fixed energy section is made of a 5-MeV/nucleon RFQ operating at 750 MHz frequency followed by another accelerator structure to be defined possibly at the same frequency as the RFQ. The variable energy section comprises a sequence of 3 GHz side-coupled linac structures. The output beam energy can be modulated by varying the rf amplitude and phase of the variable energy section. The three reference designs and a preliminary comparison of the needs of SEEIIST are given in [8].

Ion therapy linacs require a duty cycle of less than 0.1% [9]. As mentioned before, in addition to serving the ion therapy applications, in the NIMMS facility, the rest of the time, the linac can inject an ion beam into a radioisotope production line [Fig. 1(a)]. Since a higher duty cycle is required for isotope production, the NIMMS injector needs to be operated at duty cycles of about 10% with synchrotron pulses interleaved at a lower repetition rate. Acceleration at a higher duty cycle requires more elaborated cooling circuits to evacuate heat from ohmic losses due to rf surface currents. Embedding cooling circuits in turn requires more parts to be assembled in larger drift tubes, which have lower shunt impedance.

Whether the final layout for the facility is a synchrotron or a full linac, the choice of the accelerating structure after the RFQ at low energies is of particular importance for the overall beam quality. Classic drift-tube linacs (DTLs) provide strong focusing and high beam transmission; however, housing permanent magnetic quadrupoles (PMQs) inside drift tubes is costly and in a 750-MHz design particularly challenging at lower beam energies because of the small drift-tube dimensions. While classic DTL and IH-DTL structures have been extensively studied and operated by several projects [10–14], the quasi-Alvarez DTL (QA-DTL) structure developed in 1990 as part of the CERN Linac3 heavy ion injector and realized only as a scaled prototype model [15] has not been further employed since then. Its higher shunt impedance compared to classic DTL structures and the stronger focusing channel compared to IH-DTL structures make it a valid compromise worth being investigated.

The current paper has a twofold purpose: First, it describes in detail the design process of QA-DTL structures that have not received much attention in the literature so far. The aim of the design effort was to arrive at reliable parameters and cost estimates of such structures for a NIMMS facility as a basis for further decision making. Second, by doing so, this paper provides a blueprint for cavity design of DTL structures in general which could be of wider interest. In the first section, the layout and beam dynamics design process of the QA-DTL structure is presented, then the rf design is discussed in detail starting from the superperiod design, including considerations on duty cycles requiring different cooling circuit layouts, as well as magnet design. From there, the development of a full QA-DTL structure is undertaken including rf stabilization. A new technique for a reliable post-coupler design is presented that allows the analysis of the stabilization of DTL structures including QA-DTLs in electromagnetic simulations on a substructure—cell or superperiod—level, overcoming one of the main reasons why QA-DTL structures have not been considered much in the past. Based on the outcome of the design effort, a cost estimation is undertaken that completes the NIMMS QA-DTL study.

II. QA-DTL STRUCTURES

In the context of high frequency heavy ion accelerators for the NIMMS initiative, this work employs a well-defined and systematic computational approach for the design of QA-DTL structures. This design process is described in the following sections. The model not only covers the rf design but also includes the multiphysics aspects of QA-DTL cavity design such as heat analysis, mechanical deformation, and cooling system design. Having integrated all these aspects in a common model permits the rapid simulation and comparison of optimized designs at various gradients. Furthermore, a computational approach for the stabilization of QA-DTL structures is presented to make sure that the resulting designs are actually operable. The essential value of this technique is that the stabilization is analyzed in manageable electromagnetic simulations for each superperiod individually and that these provide the values for optimum post-coupler lengths. It is expected that the rf simulations are precise enough to manufacture the post couplers at their correct length without the need for a measurement-based stabilization approach as previously presented in [16].

The purpose of the NIMMS initiative at CERN is to find a cost-effective design for medical machines. As part of this framework project, the QA-DTL design study presented here analyzes the costs of such structures. Before going into the details of the study, it is essential for the reader to understand that such a cost analysis must be based on a physical implementation and thus requires an upfront knowledge in the design of such structures and that such an analysis cannot be done on the beam dynamics and electromagnetic design level alone without the idea of a concrete implementation.

The study here is based on the experience with the design of the Linac4 DTL at CERN. Precisely machined aluminum girders posed on self-supporting stainless steel tanks position drift tubes with a dedicated simple mounting mechanism inside the tanks without means for adjustment. Due to the high level of accuracy in state-of-the-art machining, this approach turned out to be cost-effective, in that it avoids any tedious alignment work after manufacturing. Drift tubes are assembled by e-beam welding and remachined to tolerances. The structure design has been described in conference publications [10,17,18]. Several institutes in the world based their designs on this mechanical design, e.g., the upcoming European Spallation Source (ESS, Lund, Sweden) [19].

At the same time that such an analysis requires an understanding of the mechanical design of the rf structure, out of experience, it does not require that the physics design of such a structure goes into all details that are required before building it. The precise tuning and the analysis of necessary tuning ranges, detailed matching from and to structures up- and downstream are not required, and some simplifications as using Slater perturbation approximations for stems in electromagnetic simulations are permitted without affecting the outcome of the study more than by few percents.

III. BEAM DYNAMICS DESIGN

A QA-DTL is a modified DTL structure with a FODO or FO..ODO..O magnet arrangement in which the distance between gaps around the magnet is typically $2\beta\lambda$. Multiple options of QA-DTL lattice arrangements are shown in Fig. 2. A long drift tube containing a quadrupole every $n\beta\lambda$ where n is the periodicity factor, $\{n \in \mathbb{N} | n \geq 3\}$, alternate with drift tubes without magnet. Featuring no magnet, these drift tubes have smaller radial dimensions which increase the achievable effective shunt impedance (ZTT) [20]. QA-DTL structures thus rely on a regular focusing scheme at lower PMQ gradients compared to classic DTL structures due to their longer distances between alternating quadrupoles [21].

The QA-DTL structures studied here for the NIMMS facility operate at 750 MHz and accelerate carbon and α particles ($A/q = 2$) from 5 to 30 MeV/nucleon at the duty cycle of 10%. The energy range, as the constraints on the input and output beam parameters, is defined in [22]. For the design of QA-DTL structures, a QA-DTL superperiod is defined in the following paragraph. In each superperiod, a total number of $(n-3)$ cells with a length of $\beta\lambda$ are sandwiched between two 1.5 $\beta\lambda$ cells. The optimum value of the periodicity factor n is a trade-off between the beam transmission and the gradient of magnets. A full QA-DTL cavity can be considered as a series of superperiods. The superperiod of the QA-DTL cavity is optimized by maximizing power efficiency as well as bringing mechanical and physical constraints within bounds. The periodicity factor of NIMMS QA-DTL cavities is set to 4. The superperiod is designed for an average axial electric field of 4 MV/m. The superperiod of a NIMMS QA-DTL structure comprises two half-length drift tubes with PMQ and two small drift tubes without magnets in-between as shown in Fig. 3.

The choice of the periodicity factor is driven by the maximum gradient achievable by the PMQs and by their length. The former parameter is dependent on the radius of the magnet, while the latter is constrained by the maximum length of the drift tube hosting it. The beam dynamics design aims to find the layout that allows for maximum (full) transmission and for PMQ gradients within the design limits. This is done by iterating over different solutions until the best compromise between aperture, periodicity factor, and transmission is found.

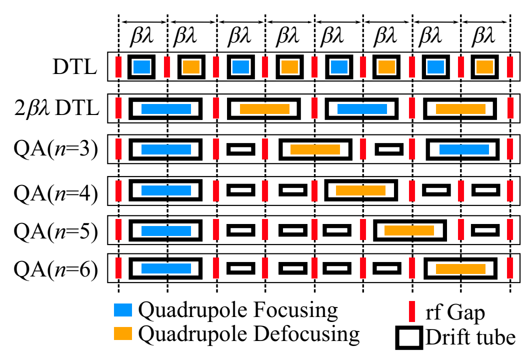

FIG. 2. A schematic illustration of various QA-DTL design options compared to classic DTL design. A long drift tube is placed every $n\beta\lambda$.

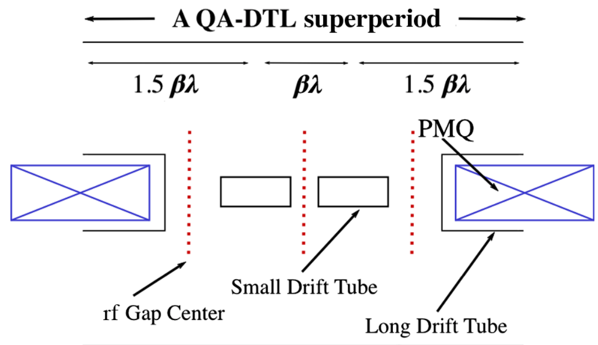

FIG. 3. A schematic illustration of the QA-DTL superperiod inside a tank (horizontal plane view). It comprises two half-length long drift tubes with PMQ and two small drift tubes without. The entire structure is designed by combining a set of these superperiods.

The main parameters of the baseline design resulting from this study are shown in Fig. 4. It can be noticed that the 6 rms envelope (corresponding to 98% of the beam profile) is kept within a 2.5-mm radius (chosen as the design aperture). The PMQ gradients are kept below 120 T/m. Adding to the 2.5-mm aperture, the estimated thickness of the drift tube, a PMQ radius of 3.5 mm can be assumed. Therefore, the maximum magnetic tip field needed along the linac would be $B_r = 0.42$ T. This value is safely within the field limit achievable by commercial PMQs, as detailed in Sec. VI. The input and output beam distributions in x-x', y-y', and φ-W planes are shown in Fig. 5.

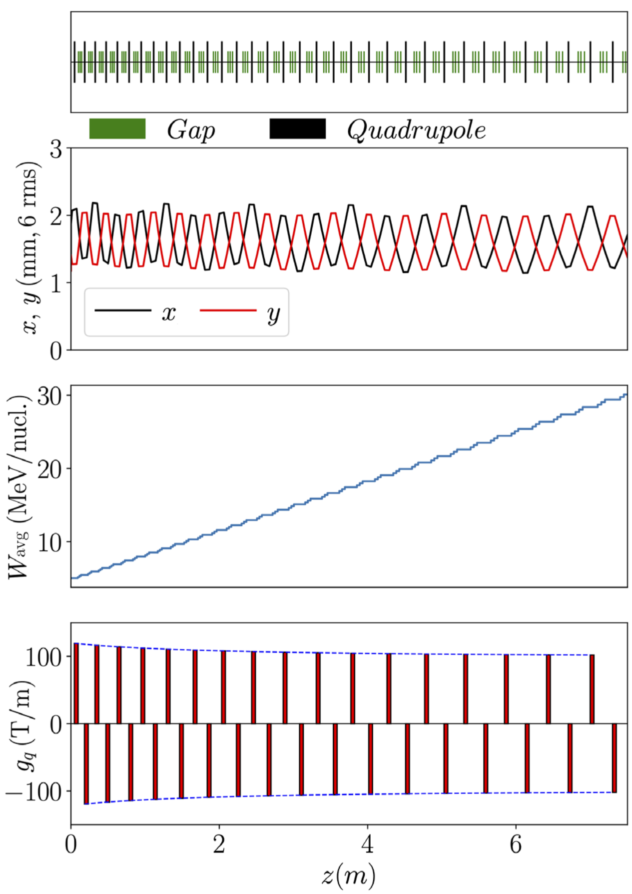

FIG. 4. From the top: the schematic of the linac (quadrupole positions in black, gap positions in green), the 6 rms x and y envelopes, the average kinetic energy, and the quadrupole gradients.

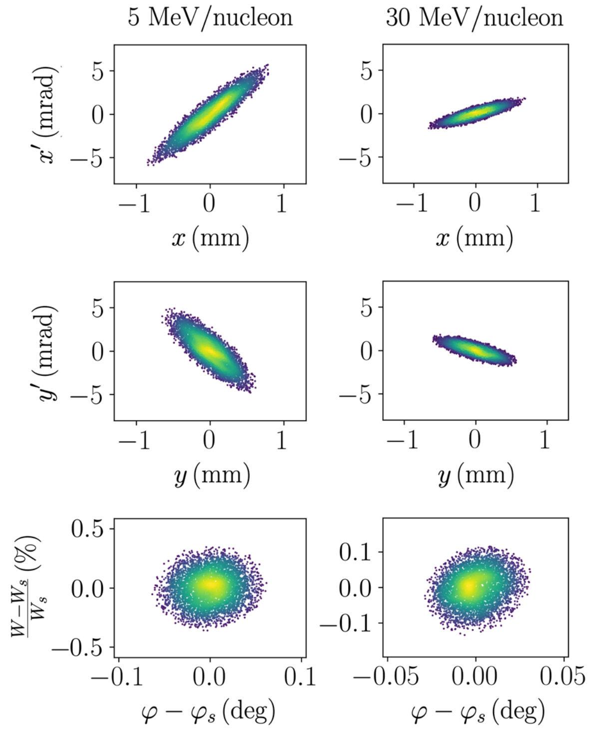

FIG. 5. Beam distributions at the entrance (5 MeV/nucleon, left diagrams) and exit (30 MeV/nucleon, right diagrams) of the full QA-DTL option. Note the different scales for the φ-W plane.

The beam dynamics design was carried out considering the full QA-DTL as a unique, stand-alone structure with an average axial field equal in all cells. This is of course an approximation used to provide the main parameters for the rf design. In order to allow for good field stability, the structure must be split into modules. The next sections describe the rf design of the first module of the QA-DTL to accelerate ions from 5 to 7 MeV/nucleon.

IV. rf DESIGN OF QA-DTL STRUCTURES

For optimizing the design, the effective shunt impedance is maximized as a measure of power efficiency. The surface electric field is restricted to 38 MV/m at maximum in the design. This value has been chosen relative to the 750-MHz RFQ mentioned before to keep breakdown rates at similar levels for these two very different structures, based on experience with the Linac4 RFQ and DTL. Dimensions of stems and drift tubes are constrained such as to foresee space for embedding PMQs and cooling circuits inside. The cross section of a half drift tube is defined by eight

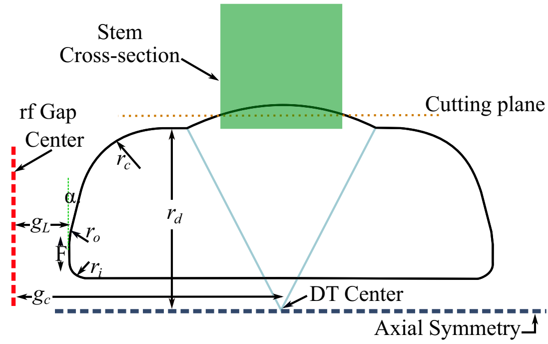

FIG. 6. A cross-sectional view of a drift tube. The drift tube is rotationally symmetric with respect to the beam axis. The geometry of a half drift tube is determined by eight parameters which are shown here. A kind of midsphere, centered on the drift tube, eases the production of the stem-to-drift-tube junction.

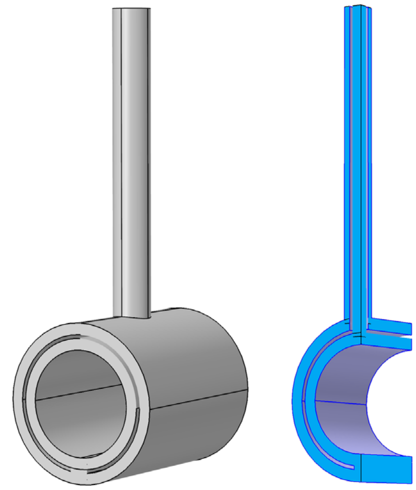

FIG. 7. Left: A 3D view of the cooling channel of a NIMMS facility structure drift tube. Right: Cooling channel cut in the symmetry planes. The area shown in blue is the water passage. Inner connections are clearly visible.

parameters as shown in Fig. 6. The stem-to-drift-tube junction has been shaped as in the Cell-Coupled Drift Tube Linac (CCDTL) design of Linac4 [23] with a kind of midsphere at the drift-tube center and to be able to manufacture the drift-tube body exclusively by lathing. Lathing achieves better surface roughness at lower costs than milling and it avoids issues with interfacing different machining techniques. A 1% increase in power loss on average in the NIMMS QA-DTL design is the price to be paid.

The rf design of the QA-DTL cavity is carried out in MATLAB. The code interacts with COMSOL Multiphysics for performing rf eigenmode calculations using the MATLAB-LiveLink interface. The code is capable of generating the 2D and 3D QA-DTL models in COMSOL and retrieving the electromagnetic fields for further postprocessing and optimization in MATLAB. The movement of the synchronous particle is studied using the Runge-Kutta ordinary differential equation solver RK45 with a variable step size [24].

Prior to the design and optimization of the superperiod of the QA-DTL structure, the dimensions of cooling circuits and PMQs need to be estimated in order to reserve the required space. In the following section, the geometry and the estimated dimensions of these elements are discussed in detail.

V. COOLING CIRCUIT OPTIONS

Depending on the duty cycle, two different options for cooling circuits have been considered to evacuate heat from the surfaces of the drift tube and the stem. At duty cycles below 1%, the heat dissipated on drift-tube surfaces can be evacuated indirectly through a stem cooling circuit. For the operation of a QA-DTL structure at duty cycles of more than 1% as required for radioisotope production, the cooling channel also needs to pass through the drift tube with PMQ to extract the heat directly and more effectively. A cooling circuit layout as used in the CERN Linac4 DTL, dimensioned for duty cycles up to 5%, is considered in this case. A 3D model of the drift-tube cooling circuit is shown on the left of Fig. 7 and a cross-sectional view is on the right. The area shown in blue represents the water passage. The stem cooling is coaxial, the drift tube is laterally fully symmetric, and the water channel is also longitudinally symmetric while the drift tube itself slightly deviates from the symmetry due to different parameters for drift-tube tips in adjacent cells.

The efficiency of the cooling circuit in the evacuation of heat on small and long drift tubes is studied using a 3D model of the first six cells of the QA-DTL structure, i.e., the first two superperiods. The model uses a set of coupled radio-frequency, heat transfer, mechanical, and fluid dynamic FEM solvers. The model calculates the rf power loss on surfaces of drift tubes, its corresponding temperature distribution, its mechanical deformation, and the pressure drop over the circuit. Here, the conductive heat transfer in metallic parts has been considered and the radiation and convection terms have been neglected. The efficiency of the cooling circuits of the second and third drift tubes to evacuate the dissipated power is shown in Fig. 8. In this study, drift tubes and stems are made from OFE copper, and they are cooled by water at a temperature of 20 °C. The power loss at the surface S is calculated using

$$P_{\text{loss}} = \frac{R_s}{2} \int |\bar{H}_t|^2 ds \qquad (1)$$

where $\bar{H}_t$ is the tangential magnetic field and R_s is the surface resistivity of copper at 750 MHz [25].

Using stem cooling has advantages due to lower mechanical complexity and consequently lower fabrication costs compared to drift-tube body cooling. However, mechanical deformation at higher duty cycles needs to

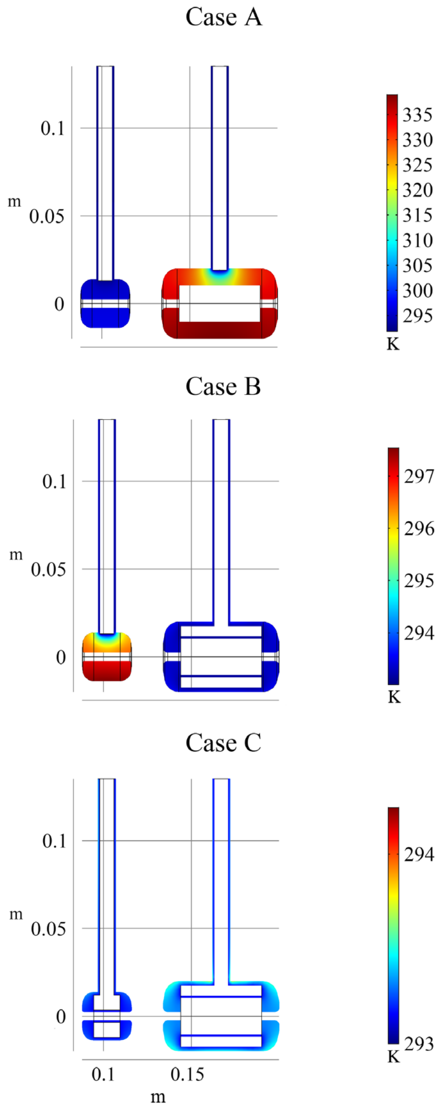

FIG. 8. A comparison of different cooling strategies on the evacuation of the heat dissipation in long and small drift tubes. The heat profile is plotted at the duty cycle of 10%. Note the different scales. Only the outer copper shell is shown, open areas contain cooling circuits and the PMQ in vacuum.

be analyzed. Three different combinations of these cooling channels in long and small drift tubes have been considered. Case A uses stem cooling circuits for both long and small drift tubes. In Case B, the cooling circuit on the long drift tube is a body circuit but stem cooling is used for small drift tubes. The power loss on small drift tubes is lower than on long drift tubes. This combination can be considered as a compromise between cooling efficiency and fabrication costs. In Case C, the drift-tube body cooling circuit is installed in all drift tubes.

For comparison, the temperature distribution on the cross section of drift tubes is plotted in Fig. 8 for all cases at a duty cycle of 10% as required for isotope production. The corresponding maximum temperature difference ΔT and displacement from the drift-tube axis Δd are listed in Table I. Since the heat dissipation on drift-tube surfaces has a linear dependency on the duty cycle, ΔT and Δd vary proportionally with the duty cycle. In the present design, the maximum allowed axis displacements for long drift tubes with PMQ, keeping full transmission is 50 μm. Naturally, this budget has to be shared with all contributors to the alignment of the magnetic PMQ axes with respect to the mechanical center of the beamline, namely the tolerance of the magnetic axis within the PMQ, the alignment of the PMQ within the drift tube, the tolerance of the drift-tube machining with respect to the tank references, and finally the alignment between rf structures. The extrapolation shows that using a stem cooling circuit for all drift tubes (case A) works up to duty cycles around 1% with a maximum temperature difference and PMQ axis displacement of about 4.8 K and 2.19 μm respectively. The maximum temperature difference at 10% duty cycle in case B is about 4.39 K. With 2.05 μm displacement, this is therefore a cost-effective solution for such duty cycles. Finally, case C can be applied at duty cycles well above 10%.

TABLE I. The maximum temperature difference and drift-tube axis displacement for all cooling strategies at a duty cycle of 10%.

	Small drift tube		Long drift tube	
	ΔT (°C)	Δd (μm)	ΔT (°C)	Δd (μm)
Case A	4.39	2.05	47.76	21.85
Case B	4.39	2.05	0.51	0.15
Case C	0.23	0.12	0.51	0.15

The deformation of long and small drift tubes in case A and case C has been compared in Fig. 9. In this plot, the duty cycle is 10% and in order to better illustrate deformed surfaces, the deformation is scaled by a factor of 300. In addition to the efficiency in heat evacuation, the dimensions of the cooling circuits are chosen such that the fluid flow is turbulent [26].

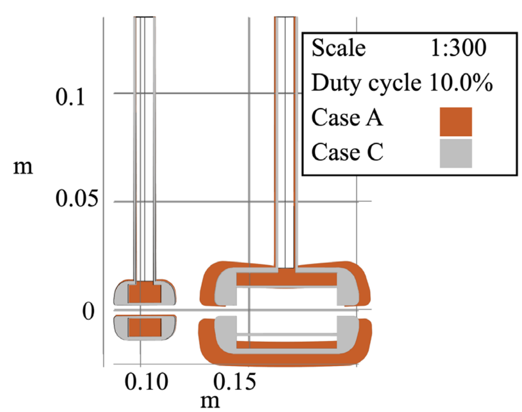

FIG. 9. The deformation of drift tubes at the duty cycle of 10%. Case A uses stem cooling in all drift tubes and case C uses drift-tube cooling. The deformation is scaled by a factor of 300 for better illustration.

VI. PMQ DIMENSIONING

In the design of the QA-DTL structure, the long drift tubes need to accommodate the PMQ, and magnet dimensions need to be defined early in the design process. In the present study, a 16-segment Halbach-type PMQ is considered. A schematic arrangement of magnetic blocks and their easy-axis direction is shown in Fig. 10. The parameters r_i and r_o are the inner and outer radius of the PMQ. The easy axis of magnetization in each segment is rotated by 45° with respect to its next neighbor. The magnetic field gradient close to the axis of the PMQ is expressed by

$$B' = 2B_r K\left[\frac{1}{r_i} - \frac{1}{r_o}\right] \quad K = \cos^2\left(\frac{\pi}{M}\right)\sin\left(\frac{2\pi}{M}\right)\frac{M}{2\pi}, \tag{2}$$

where B_r and M are the remanent magnetic field of each segment and the total number of segments, respectively [27,28]. For a 16-segment magnet, K is equal to 0.94. The magnetic alloy of the PMQ segments is assumed to be Samarium Cobalt 95 with a remanent field of 0.95 T, the same material as used in the Linac4 DTL [29]. The supporting frame for the magnet is foreseen to be made from non-magnetic stainless steel with a minimum thickness of 2.0 mm.

Using the 2D approximation to calculate the magnetic gradient based on known PMQ dimensions is straightforward and quick. However, the profile of the magnetic field is different compared to the real finite length PMQ due to the fringe field. A 3D model is used to calculate the effect of the fringe field on the magnetic gradient along the axis of a 16-segment PMQ. In this example, the inner and outer radius of the PMQ is set to 3.5 and 10 mm, respectively, and the length of the PMQ is 50 mm. The results are plotted in Fig. 11. In this particular example, the relative difference in integrated gradient between the full 3D model and the 2D approximation is about 1.6%.

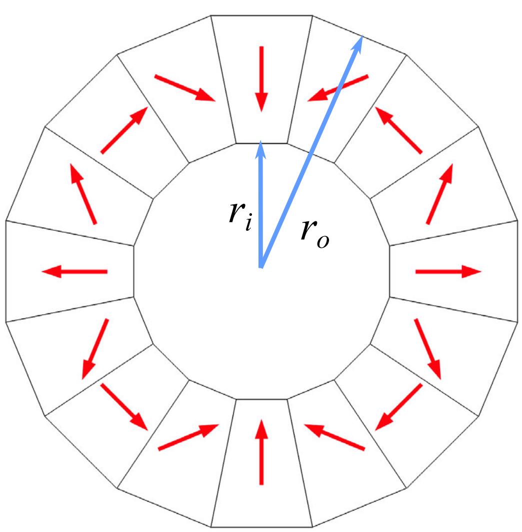

FIG. 10. A schematic arrangement of magnetic blocks and easy-axis direction of a 16-segment PMQ.

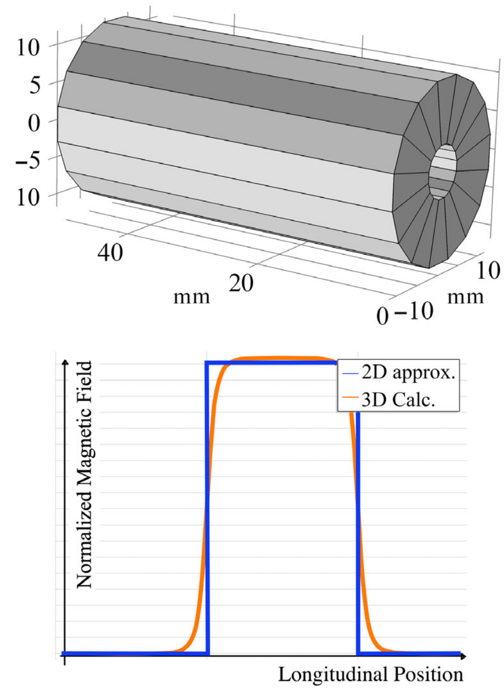

FIG. 11. Top: 3D model of the PMQ. Bottom: Comparison of the 3D simulation results to the 2D approximation of the magnetic field of the PMQ.

VII. QA-DTL SUPERPERIOD OPTIMIZATION

In this section, the optimization of the general design parameters of an average superperiod of the QA-DTL structure is discussed in detail. While in a classic DTL, the optimization of a single cell at average beam energy is sufficient, in a QA-DTL, it is practical to optimize a full superperiod at once. The optimization process aims at maximizing the average effective shunt impedance under the following constraints: the maximum surface electric field must be lower than 38.0 MV/m, enough space for embedding a PMQ and cooling circuits in drift tubes must be available, enough space for fitting stems on drift tubes needs to be provided and finally the rf frequency needs to be kept at the design frequency. The bore radius of all drift tubes is fixed at 2.5 mm. The range of radii of long drift tubes r_L is constrained between 20 and 25 mm, and of small drift tubes r_S is between 10 and 18 mm. The radius of 20 mm for long drift tubes corresponds to the minimum radius required for embedding a PMQ and cooling circuits, and 10.0 mm is the minimum radius required for housing the cooling channel inside the small drift tubes. The radius of the stem is set to 6.0 mm at which there is enough space available for embedding the two water cooling channels inside the stems.

The superperiod parameters are optimized at an average beam energy of the cavity, 6.0 MeV/nucleon in the NIMMS design. The phase of the synchronous particle is −20° for all cells. The energy gain is found by tracking the synchronous particle along the beam axis through the full superperiod. With the energy gain, the shunt impedance ZTT_{sp} can be calculated for the full super-period. Several assumptions have been made on the geometry of drift tubes, minimizing the number of geometrical parameters and lowering the computation time. For the optimization of the superperiod, small drift tubes have the same geometrical parameters except for their length. The same assumption is made for the two bigger half-length drift tubes. Furthermore, the effect of stems on frequency shift and power loss is ignored in the optimization stage to perform rf calculations using axially symmetric conditions.

It is important to understand that the superperiod design cannot be precisely split into meaningful individual cells with uniquely defined cell boundaries. For example, analyzing the FEM model of a substructure of just a single gap with two half drift tubes is not fully representative of the actual field distribution as the resulting electromagnetic structure with the respective (perfect electric conductor) boundary conditions so investigated will considerably deviate from the one situated within the superperiod. As a corollary, since the boundary is not uniquely defined, also the power loss of that individual cell could not be assigned correctly and thus any calculation of a shunt impedance for that individual cell will remain ambiguous.

VIII. GLOBAL QA-DTL OPTIMIZATION

Since there is no prior knowledge on the location of possible minima, the superperiod of the QA-DTL cavity is optimized using two different algorithms independently: random search (RS) and genetic algorithms (GA). The results of both algorithms are presented and compared.

In random search (RS), each solution is a one-dimensional array of 16 elements containing geometrical parameters of the QA-DTL superperiod such as the diameter of drift tubes, face angle, etc. A total number of about 10,000 random solutions has been used. For illustration, the randomly generated solutions have been sorted in two dimensions based on the radius of small r_S and long r_L drift tubes, as shown in Fig. 12. The results in the diagram are filtered based on the rf efficiency and geometrical feasibility. All results with ZTT_{sp} lower than 95.0 MΩ/m, and with a maximum surface electric field higher than 38 MV/m, are ignored. Drift tubes in all solutions which are located in the gray area are big enough to house a PMQ and cooling circuits inside. The maximum ZTT_{sp} for $r_L > 20$ mm is 96.5 MΩ/m.

In the genetic algorithm (GA) setup that has been employed, a population of about 30 solutions has been used in the evolution process of GA optimization. The heuristic crossover operator and the tournament selection method are used by the GA module [30,31]. The cross-over rate is set to 80% and the contribution of the elites is set at

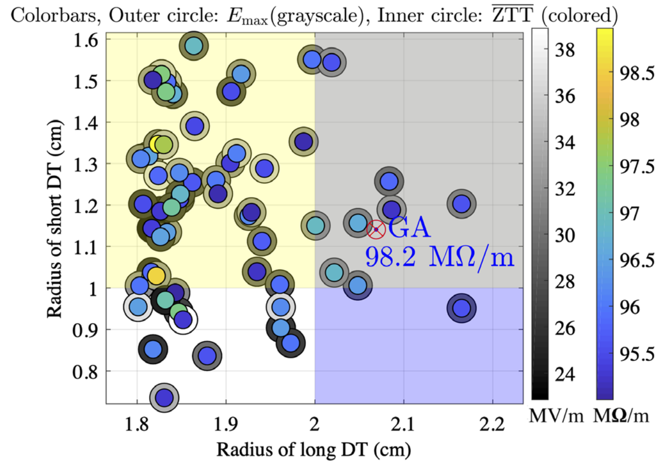

FIG. 12. Distribution of valid solutions obtained by a random search among 10,000 randomly generated parameter sets. All solutions with ZTT_{sp} higher than 95.0 and a maximum surface electric field below 38 MV/m are plotted. The result of the genetic algorithm is shown as a red cross.

7% of the population. As is shown in Fig. 12, the optimum obtained by GA is close to the one found by RS but the ZTT_{sp} is about 2% higher.

IX. FULL QA-DTL CAVITY DESIGN

In this section, the design of the full QA-DTL structure is discussed. The design procedure of the full QA-DTL cavity is based on constructing superperiods one by one, starting from the low energy end of the cavity. At this design stage, each superperiod is constructed with general parameters like radii and other radial dimensions, as well as dimensions required for housing PMQs and cooling circuits found in the superperiod optimization. This generalization is required to limit the complexity of cavity manufacturing. However, the length of cells needs to increase with the particle velocity β and the longitudinal parameters of drift tubes (gap lengths and face angles) need to be adjusted and optimized for high rf efficiency with the same optimization criteria as for the average superperiod such that the resonant frequency of the superperiod remains at the design frequency of 750 MHz.

Since stems cannot be modeled in 2D FEM calculations, their resonant frequency shift has been estimated using the Slater perturbation theorem [32]. All superperiods of the QA-DTL cavity are designed for the same average axial electric field level. For the initial design, the synchronous phase of all cells is fixed at $-20°$. The synchronous particle accelerated by the axial electric field is tracked through the superperiod. The synchronous phase of all cells is adjusted by a shift of gap centers, to the design value with a relative error of $\pm 0.05\%$. This process is performed for all superperiods successively until the final beam energy is reached.

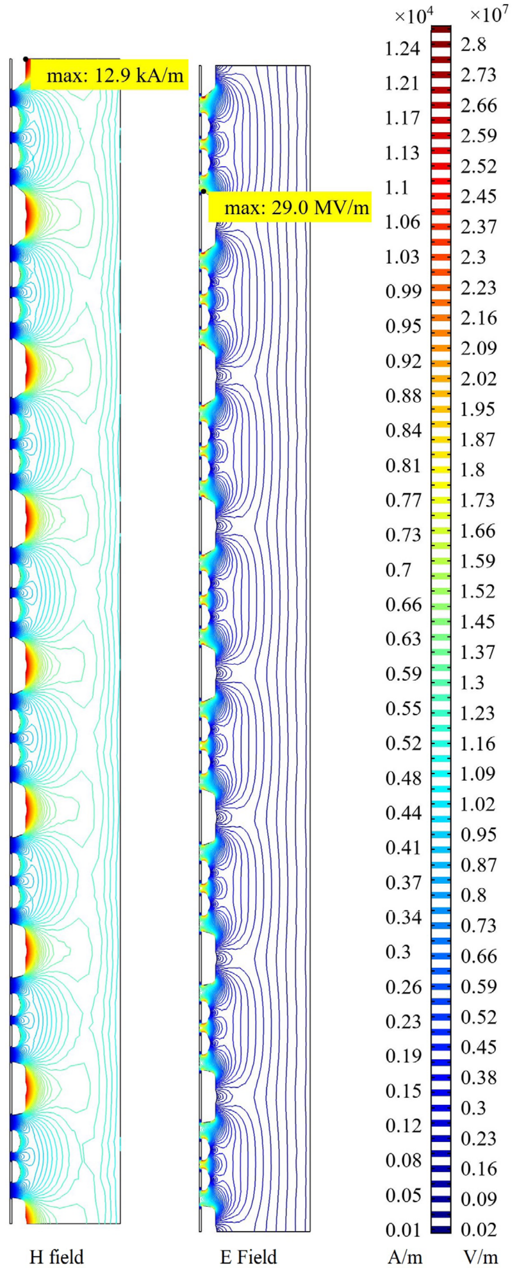

FIG. 13. A cross-sectional view of electric and magnetic field distribution in a QA-DTL cavity at 4 MV/m.

TABLE II. Parameters of NIMMS QA-DTL cavity.

Average axial electric field	4 MV/m
Beam energy$_{in}$	5 MeV/nucleon
Beam energy$_{out}$	7.02 MeV/nucleon
Cavity length	1.4 m
Peak power	160 kW
Peak current	0.2 mA
Maximum surface E-field	29 MV/m
Number of big/small drift tubes	8/16
ZTT big/small cells	100..110/170..180 MΩ/m
Number of PMQs	7

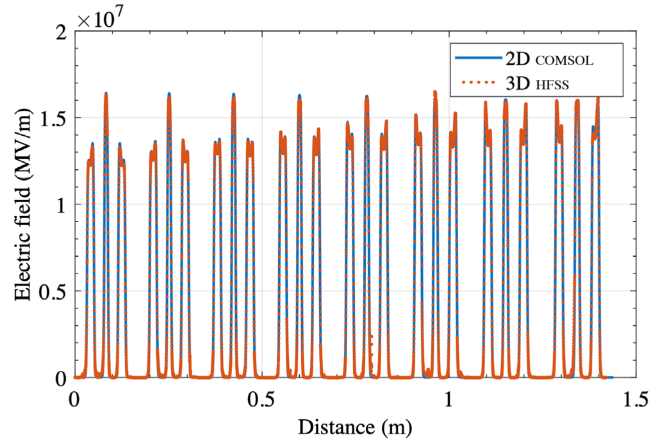

FIG. 14. Comparison of the axial electric field profile of the QA-DTL at 4 MV/m obtained in 2D COMSOL and 3D HFSS simulations.

X. RESULTS OF THE QA-DTL DESIGN

The results of the design of the NIMMS QA-DTL cavity at an average axial electric field of 4 MV/m are presented in this section. The cavity comprises 24 drift tubes in which 8 drift tubes are long with a radius of 20 mm. The radius of the small drift tubes is 11 mm. The cavity has an inner diameter of about 273 mm and is about 1.4 m long. The cross-section of the cavity and the electric and magnetic field contours are shown in Fig. 13. The maximum surface electric field is about 29.0 MV/m. The effective shunt impedance ZTT of longer and smaller cells in the structure is roughly between 100..110 MΩ/m and 170..180 MΩ/m, respectively. The numbers have been found by splitting the cells at their nominal boundary. The higher effective shunt impedance of small cells is because of lower loss on small drift-tube surfaces. However as mentioned earlier, this splitting is not unique. The physical characteristics and figures of merit of the cavity are listed in Table II.

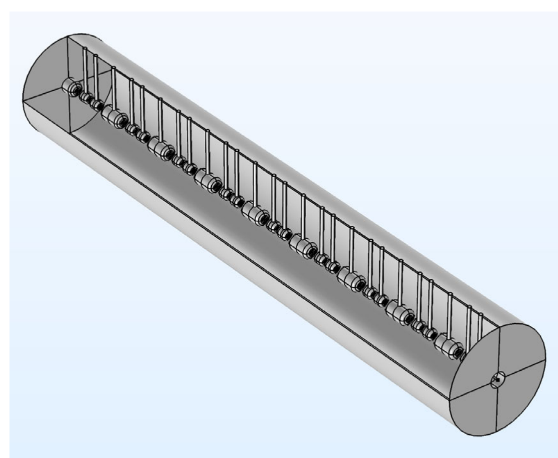

FIG. 15. The 3D model of the NIMMS QA-DTL tank design at 4 MV/m.

The electromagnetic field distribution in the QA-DTL cavity has been calculated using 2D COMSOL and 3D HFSS eigenmode solvers. The axial field profiles calculated by both solvers are shown in Fig. 14. The average axial field of all cells is distributed uniformly with a relative error of $\pm 2.0\%$ around the average value. The final QA-DTL cavity is shown in Fig. 15.

XI. STABILIZATION

Axial field stabilization using passive $\lambda/4$ post couplers is a necessity for the NIMMS QA-DTL design because such structures are expected to be susceptible to field variations due to static and dynamic effects like manufacturing tolerances, active tuning, thermal expansion, or beam loading. Post couplers are a chain of resonating elements that can couple with the cavity resonators and in consequence, the stability of fields in the operation mode increases. Post couplers and their working principle are amply discussed in the literature [33–36].

A practical procedure for accurate adjustments of post couplers has been applied to CERN's Linac4 DTL cavities previously [16]. This technique is straightforward for the experimental adjustments of post couplers. While the authors successfully applied it also in numerical simulations, there is a major difficulty with long Alvarez type cavities since they require high computing resources due to their overall volume to be meshed and the fine mesh granularity required to correctly represent a considerable number of small elements inside such as drift tubes and stems. For measuring the tilt-sensitivity parameters of the cells, several optimization attempts need to be made to adjust the perturbation to the desired frequency shift [37]. In addition, to find the reference length of the post coupler, the resonant frequency shift needs to be calculated for each post coupler individually [16].

A new procedure based on modal analysis of the highest post-coupler modes and its equivalent circuit model for the stabilization of NIMMS quasi-Alvarez structures has been established which will be discussed in the following section. The new method extracts post-coupler lengths using the simulation of QA-DTL superperiods (single cells for classic DTL structures) sequentially using a 3D model in the design stage. The method is applicable to DTL structures in general. In the following section, the physics behind the stabilization technique is discussed briefly and the procedure of post-coupler tuning is presented. In addition, the results of the post-coupler stabilization of the whole QA-DTL structure at 4 MV/m are discussed. For the sake of simplicity in the following, stems are not included in the 3D simulations. This is acceptable as their resonances are considerably lower than those of the post couplers, they stand orthogonal to the field lines in the relevant modes, and their frequency and loss effect can be estimated by Slater perturbation.

XII. NUMERICAL TECHNIQUE FOR POST-COUPLER ADJUSTMENT

DTL cavities equipped with post couplers form biperiodic structures [38]. Two modal branches in the dispersion diagram belong to the TM_{01x} and the post coupler (PC) resonances. As discussed in the literature, by deliberate adjustment of post-coupler lengths, the PC mode branch can be brought close to the TM_{01x} mode branch, leading to a coupling between the modal spectra. While this confluence of modal spectra can easily be achieved on average, it is however not enough for proper stabilization over all the cavity. By the analysis of tilt sensitivity measurements, it has been understood since the beginning that the stabilization can and needs to be achieved on a cell-by-cell basis. In the following, it is shown that corresponding modes can be simulated for each cell (or superperiod in the case of the QA-DTL) and that by the coincidence of modes on a cellular granularity, stabilization is achieved.

It is the usual practice to design DTL structures cell by cell starting from the low energy end. To find the TM modes and more specifically the main accelerating mode TM_{010}, the cell is simulated with perfect electric conductor (PEC) boundary conditions. Since excited post couplers have no perpendicular electric fields at the cell boundary, post-coupler modes cannot be studied with PEC cell boundaries. Instead, perfect magnetic conductor (PMC) cell boundaries need to be applied to study PC modes. As is well known, PMC surfaces do not physically exist, but it is possible to define them numerically, and they physically make sense when corresponding symmetry conditions are to be established in a model. This same technique has been used on a full DTL structure previously in order to find the PC_0 mode in the dispersion diagram [39]. Due to the conducting cavity end walls, the PC_0 mode is actually a forbidden mode in the physical cavity, whose coincidence with the TM_{010} mode nevertheless establishes the confluence of modal branches. The difference here to that previous work is that, as mentioned before, the coincidence of modes is established on a cell-by-cell basis, and it is shown that this is what leads to full stabilization with a low local tilt sensitivity slope in all the cavity.

The electric field distribution of the post-coupler mode of a QA-DTL superperiod equipped with PCs is shown in Fig. 16. In the figure, the normalized intensity of $E_{\|}$, which is the only component of the electric field due to the coincident boundary condition, is shown in color and the direction of the electric field is plotted as white arrows. As can be seen in the figure, a considerable fraction of the electromagnetic energy is stored around the post coupler and the rest is stored in the area between the drift tube and the cylindrical wall. With the capacitance between the drift tube and the cylindrical cavity wall C', and the equivalent inductance and capacitance of the post coupler L'' and C'', respectively, the equivalent circuit representation of the post-coupler mode can be modeled as in Fig. 16(c).

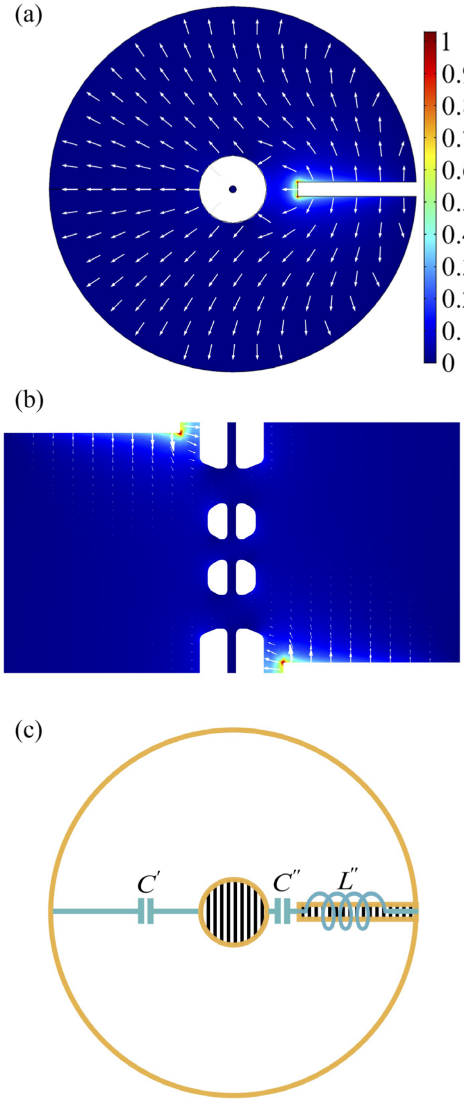

FIG. 16. (a) The electromagnetic field distribution in the cell boundary plane cutting through a post coupler. The intensity of the electric field is shown by colors normalized to one. Arrows show the direction of the electric field. (b) Corresponding horizontal cross-section with the same scaling. (c) The equivalent circuit of the PC_0 mode of the post coupler.

This branch has been identified as the coupling admittance Y' in [16],

$$Y' = j\omega C' + \frac{j\omega C''}{1 - \omega^2 L'' C''} \tag{3}$$

with resonance frequency $\omega' = 1/\sqrt{L''}\sqrt{(1/C' + 1/C'')}$. Due to symmetry conditions valid for the basic post-coupler mode, there is no excitation via the branch of the drift tubes. It has been shown in [16] that this formula corresponds to the local tilt-sensitivity slope. Therefore, the post coupler stabilizes locally at a frequency of ω'. Since the cavity operates at the frequency of ω_{op}, the post-coupler length should be set

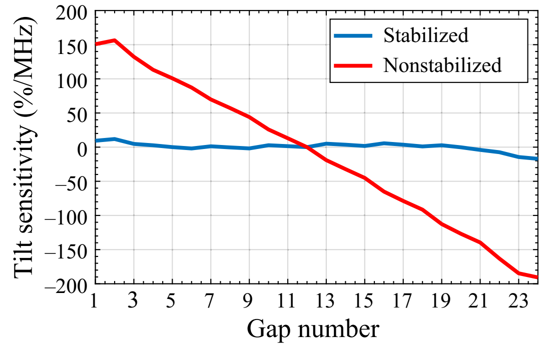

FIG. 17. Tilt sensitivity of stabilized and nonstabilized NIMMS QA-DTL at 4 MV/m.

to its proper length at which $\omega' = \omega_{op}$ and then the PC_0 mode couples to the TM_{010} mode.

The procedure of stabilization of the whole structure can be performed by adjusting the local tilt-sensitivity slope in each cell or superperiod successively. The procedure of stabilization is as follows: (i) For the first superperiod, move both post couplers uniformly until the resonance frequency of PC_0 be equal to the operation one $\omega' = \omega_{op}$. (ii) Starting from the second cell, adjust the post coupler at the lower energy side of the superperiod to the length obtained from the previous superperiod stabilization. (iii) Move the post coupler at the higher energy end of the super period until the $\omega' = \omega_{op}$. (iv) Repeat (ii) and (iii) for all superperiods consequently until all post couplers have been set.

All post couplers of the NIMMS QA-DTL have been adjusted using this procedure. The tilt sensitivity calculations reveal that when all post couplers are out, the tilt sensitivity of the cells is distributed between $\pm 160\%$/MHz. After adjusting the post couplers, the tilt sensitivity of cells improves to a range between $\pm 5\%$/MHz as shown in Fig. 17. The diameter of all post couplers is 1 cm, and the individual gaps between the post coupler and the corresponding drift tube, for all nine post couplers from the low to the high energy end of the structure, are 3.32, 3.32, 3.38, 3.39, 3.44, 3.45, and 3.5 cm.

XIII. COST ESTIMATION

As mentioned earlier, minimizing the costs of the medical facility is essential for reducing the treatment price. In the following section, the cost analysis of the QA-DTL structure for the synchrotron injector is summarized. The goal of such a study is not only to estimate the costs of QA-DTL structures but also to understand the sensitivity of the costs with respect to the different factors. This study is essential to make well-founded decisions on the optimum parameters of the QA-DTL structures for the full linac option.

The total costs of several QA-DTL structures are compared for different average axial electric fields ranging from 2 to 8 MV/m. The particle energy for all cases varies between 5 and 7 MeV/nucleon and the duty cycle is 10%. Designs at lower electric fields yield longer structures. The construction costs approximately vary linearly with respect to the length of the structure. In contrast, the ohmic losses go down with lower electric fields. The required rf power varies quadratically with the electric field. The overall costs of the QA-DTL structure analyzed in the present work consist of the construction costs C_C and costs relative to the rf power station C_P.

The analysis is based on the mechanical structure and related experience from the construction of the Linac4 DTL cavities [10]. The components considered in the present cost study are drift tubes, PMQs, tuners, post couplers, girders, tanks, end walls, the power coupler, and the rf window. Included are expenses for material, machining, welding, copper plating, heat treatments, metrology, assembly, tuning, and stabilization, as well as vacuum equipment, and tests. In the cost estimation, however, infrastructure costs and accelerator commissioning that are relatively independent of the actual structure have not been included and therefore the cost estimates do not reflect the full costs related to the structure in a NIMMS-type facility. The sensitivity of the total construction cost of a QA-DTL structure for two different average axial electric field values is shown in Fig. 18. Lowering the electric fields raises the costs for drift tubes by about 50%, PMQs by about 20% and tuner and post couplers about 70%, while the contribution of other parts is only a few percent.

Besides the construction costs, the high-power rf station has a significant contribution to the overall costs. Several options have been proposed for the power source such as klystrons, inductive output tubes (IOTs), and solid state amplifiers (SSAs). Since commercial klystrons are only available at a frequency of 704 MHz, IOTs and SSAs are the considered power sources at 750 MHz in the first place. In the long term, the use of SSAs is economically interesting mainly due to its lower maintenance costs and higher operational reliability related to the absence of high voltage. However, also efforts in making klystrons more efficient have been intensified in recent years [40,41].

Considering costs for SSAs in recent projects at CERN, the estimated price per peak output power is about 10 EUR/W. At that price, facility costs are dominated by the costs for the rf source. As the price per watt of SSA output power has been falling over the last decade, the calculation has been repeated for two more cases at 5 EUR/W and 2 EUR/W. The aim of these calculations is to study the sensitivity of the overall costs of rf power sources with respect to different options and to provide a basis for decision making while making the study independent from the technology. A 750-MHz rf source with such an optimistic price may not exist at the moment.

Being independent of the technology, this cost comparison also does not reflect well the situation of klystrons which are available on the market at discrete nominations of frequency and power, and where rather the structure or potentially a series of structures needs to be adapted to the available power source. Their use is only comparable if the maintenance, downtime, and replacement costs are taken into account over a comparable lifetime. A high-voltage power modulator is required in addition to run the equipment, and running an installation with just one or two klystrons might require some maintenance overhead. Nevertheless, shifting the operating frequency to a frequency at which commercial klystrons are available could be considered on one hand, however, with repercussions on the rest of the machine. On the other hand, this analysis may help justify developing cheaper commercial rf power sources for medical purposes in view of the expected need for several ion therapy centers worldwide in the future.

The cost comparison at different gradients is plotted in Fig. 19. At rf power costs of 10 EUR/W, the expenses for rf

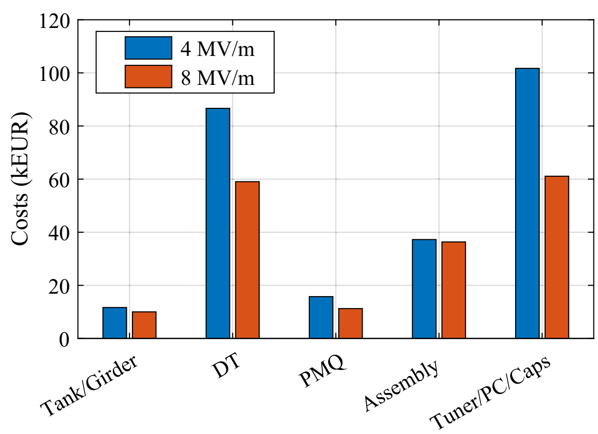

FIG. 18. A comparison of construction costs of different parts of a QA-DTL at the two values of an average axial electric field of 4 MV/m (blue) and 8 MV/m (red).

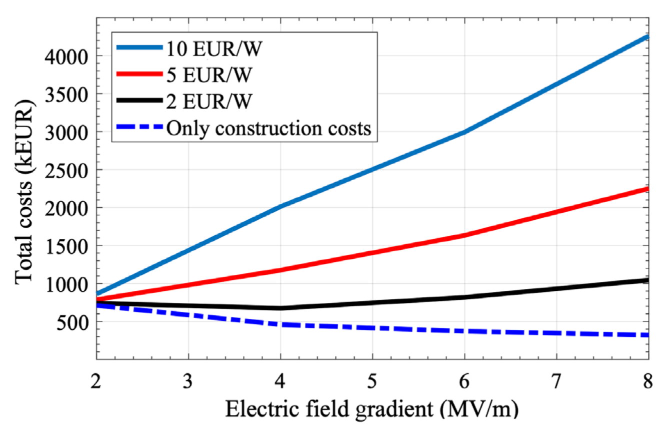

FIG. 19. The estimated total costs (construction and rf power source costs) of NIMMS QA-DTL as a function of the average axial electric field. The calculation has been performed based on three different rf costs of 2, 5, and 10 EUR/W. The dashed line shows only the costs related to the construction of the structure.

power sources dominate the construction costs and it is reasonable to construct the linac at a lower gradient. Considering rf costs of 5 EUR/W leads to a 40% reduction of the total cost at the average axial electric field level of 4 MV/m, and the rate of power cost variation with respect to the gradient is lower. For the case of 2 EUR/W, the cost variation is about zero at an average axial electric field of 4 MV/m and the total cost is minimum. From this study, one can conclude that reducing costs for high power rf sources is crucial for building cost-effective machines.

XIV. CONCLUSIONS

QA-DTL structures have been studied for a future NIMMS heavy ion therapy facility. After a short introduction to the NIMMS machines and previous QA-DTL designs, this manuscript details the design considerations that are required to arrive at reliable cost estimates. Starting at duty-cycle considerations with general design decisions on cooling circuits and PMQs, it describes the optimization of the average QA-DTL superperiod and the iterative development of a complete linac structure. The manuscript describes a new technique for post-coupler stabilization as required for such long DTL structures. The full design procedure outlined here may serve as a blueprint for the design of DTL structures in general. Based on this procedure, several QA-DTL designs are evaluated with respect to their costs at different accelerating gradients, and the importance of choosing a cost-effective rf source is underlined.

[1] M. Vretenar, V. Bencini, M. R. Khalvati, A. Lombardi, D. Tommasini, E. Benedetto, M. Sapinski, and Y. Foka, The Next Ion Medical Machine Study at CERN: Towards a next generation cancer research and therapy facility with ion beams, in *Proceedings of IPAC'21, Campinas, SP, Brazil* (JACoW, Geneva, Switzerland, 2021), pp. 1240–1244, 10.18429/JACoW-IPAC2021-MOPAB413.

[2] D. Raghavan, M. S. Ahluwalia, C. D. Blanke, J. Brown, E. S. Kim, G. H. Reaman, and M. A. Sekeres, *Textbook of Uncommon Cancer* (John Wiley & Sons, New York, 2017), 10.1002/9781119196235.

[3] C. P. Karger and P. Peschke, RBE and related modeling in carbon-ion therapy, Phys. Med. Biol. **63**, 01TR02 (2017).

[4] A. Garonna, U. Amaldi, R. Bonomi, D. Campo, A. Degiovanni, M. Garlasché, I. Mondino, V. Rizzoglio, and S. Verdú Adrés, Cyclinac medical accelerators using pulsed C^{6+}/H_2^+ ion sources, J. Instrum. **5**, C09004 (2010).

[5] A. Kitagawa, T. Fujita, M. Muramatsu, S. Biri, and A. G. Drentje, Review on heavy ion radiotherapy facilities and related ion sources, Rev. Sci. Instrum. **81**, 02B909 (2010).

[6] U. Amaldi, M. Dosanjh, B. Singers Sørensen, M. Scholz, J. Balosso, J. Overgaard, and S. Rossi, A facility for tumour therapy and biomedical research in South-Eastern Europe, *CERN Yellow Reports: Monographs* (CERN, Geneva, 2019), 10.23731/CYRM-2019-002.

[7] M. R. Zalutsky and M. Pruszynski, Astatine-211: Production and availability, Curr. Radiopharm. **4**, 177 (2011).

[8] E. Benedetto, U. Amaldi, V. Bencini, M. Dosanjh, Y. Foka, D. Kaprinis, M. R. Khalvati, A. Lombardi, M. Sapinski, M. Vretenar, and X. Zhang, Comparison of accelerator designs for an Ion Therapy and Research Facility, CERN, Geneva, Technical Reports No. CERN-ACC-NOTE-2020-0068, No. NIMMS-Note-001, 2020, https://cds.cern.ch/record/2748083.

[9] A. Degiovanni and U. Amaldi, Proton and carbon linacs for hadron therapy, in *Proceedings of the 27th International Linear Accelerator Conference, LINAC2014, Geneva, Switzerland* (JACoW, Geneva, Switzerland, 2014), pp. 1207–1212, https://accelconf.web.cern.ch/LINAC2014/papers/friob02.pdf.

[10] S. Ramberger, P. Bourquin, A. Cherif, Y. Cuvet, A. Dallocchio, G. Favre, J.-F. Fuchs, J.-M. Geisser, F. Gerigk, J.-M. Giguet, J. Hansen, M. Polini, S. Sgobba, N. Thaus, and M. Vretenar, CERN Linac4 drift tube linac manufacturing and assembly, in *Proceedings of the 27th International Linear Accelerator Conference, LINAC2014, Geneva, Switzerland* (JACoW, Geneva, Switzerland, 2014), pp. 923–925, https://accelconf.web.cern.ch/LINAC2014/papers/thpp036.pdf.

[11] M. Lindroos, S. Molloy, D. McGinnis, C. Darve, and H. Danared, The ESS linac design, in *Proceedings of 26th International Linear Accelerator Conference, LINAC2012, Tel-Aviv, Israel* (JACoW, Geneva, Switzerland, 2013), pp. 768–772, https://accelconf.web.cern.ch/LINAC2012/papers/th2a01.pdf.

[12] R. Hardekopf, Progress in design of the SNS linac, in *Proceedings of 15th Meeting of the International Collaboration on Advanced Neutron Sources*, KEK (KEK, Tsukuba, 2001), pp. 197–212, https://inis.iaea.org/search/search.aspx?orig_q=RN:33009985.

[13] Y. Iwata *et al.*, Alternating-phase-focused IH-DTL for heavy-ion medical accelerators, in *Proceedings of the 10th European Particle Accelerator Conference, Edinburgh, Scotland, 2006* (EPS-AG, Edinburgh, Scotland, 2006), pp. 2328–2330, https://accelconf.web.cern.ch/e06/PAPERS/WEPCH169.PDF.

[14] C. Zhang, H. Podlech, U. Ratzinger, and R. Tiede, Efficient solution for accelerating very high intensity beams in the low and medium energy regime, Phys. Rev. Accel. Beams **22**, 100101 (2019).

[15] H. Haseroth, A heavy ion injector at CERN, CERN, Geneva, Technical Report, 1990, https://cds.cern.ch/record/217110.

[16] M. R. Khalvati and S. Ramberger, Straightforward and accurate technique for post-coupler stabilization in drift tube linac structures, Phys. Rev. Accel. Beams **19**, 042001 (2016).

[17] S. Ramberger, N. Alharbi, P. Bourquin, Y. Cuvet, F. Gerigk, A. M. Lombardi, E. Sargsyan, and M. Vretenar, Drift tube linac design and prototyping for the CERN Linac4, *Proceedings of the 24th Linear Accelerator Conference LINAC08, Victoria, BC, Canada* (JACoW, Geneva, Switzerland, 2008), pp. 184–186, https://accelconf.web.cern.ch/LINAC08/papers/mop049.pdf.

[18] I. Sexton, T. Tardy, J.-M. Geisser, A. Cherif, F. Mirapeix, Y. Cuvet, S. Ramberger, G. Favre, and S. Sgobba, The drift

tube welding assembly for the Linac4 drift tube linac at CERN, in *Proceedings of the 27th International Linear Accelerator Conference, LINAC2014, Geneva, Switzerland* (JACoW, Geneva, Switzerland, 2014), pp. 929–931, https://accelconf.web.cern.ch/LINAC2014/papers/thpp038.pdf.

[19] P. Mereu, M. Mezzano, M., F. Grespan, A. Pisent, M. Poggi, C. Roncolato, D. Castronovo, and R. Visintini, ESS DTL mechanical design and prototyping, in *Proceedings of 28th International Linear Accelerator Conference, LINAC16, East Lansing, MI* (JACoW, Geneva, Switzerland, 2016), pp. 2131–2133, 10.18429/JACoW-IPAC2016-WEPMB008.

[20] J. M. Garland, J.-B. Lallement, and A. Lombardi, LINAC5–a quasi-Alvarez linac for BioLEIR, J. Phys. Conf. Ser. **874**, 012057 (2017).

[21] D. J. Warner, Heavy ion acceleration using drift-tube structures with optimised focusing, in *Proceedings of the 1988 Linear Accelerator Conference, Williamsburg, VI* (Continuous Electron Beam Accelerator Facility, Newport News, VI, 1988), pp. 109–111, https://accelconf.web.cern.ch/l88/papers/mo3-26.pdf.

[22] V. Bencini, H. W. Pommerenke, A. Grudiev, and A. M. Lombardi, 750 MHz radio frequency quadrupole with trapezoidal vanes for carbon ion therapy, Phys. Rev. Accel. Beams **23**, 122003 (2020).

[23] M. Vretenar, Y. Cuvet, G. De Michele, F. Gerigk, M. Pasini, S. Ramberger, R. Wegner, E. Kenzhbulatov, A. Kryuchkov, E. Rotov, A. Tribendis, and M. Naumenko, Development of a cell-coupled drift tube Linac (CCDTL) for Linac4, *Proceedings of the 24th Linear Accelerator Conference LINAC08, Victoria, BC, Canada* (JACoW, Geneva, Switzerland, 2008), pp. 67–69, https://accelconf.web.cern.ch/LINAC08/papers/mop008.pdf.

[24] T. E. Simos, A Runge-Kutta Fehlberg method with phase-lag of order infinity for initial-value problems with oscillating solution, Comput. Math. Appl. **25**, 95 (1993).

[25] D. M. Pozar, *Microwave Engineering* (John Wiley & Sons, New York, 2009), https://www.wiley.com/en-us/Microwave+Engineering,+4th+Edition-p-9780470631553.

[26] J. H. Lienhard IV and J. H. Lienhard V, *A Heat Transfer Textbook* (Phlogiston Press, Cambridge, MA, 2005), https://ahtt.mit.edu.

[27] K. Halbach, Design of permanent multipole magnets with oriented rare earth cobalt material, Nucl. Instrum. Methods **169**, 1 (1980).

[28] J. K. Lim, P. Frigola, G. Travish, J. B. Rosenzweig, S. G. Anderson, W. J. Brown, J. S. Jacob, C. L. Robbins, and A. M. Tremaine, Adjustable, short focal length permanent-magnet quadrupole based electron beam final focus system, Phys. Rev. ST Accel. Beams **8**, 072401 (2005).

[29] F. Gerigk, M. Vretenar *et al.*, *Linac4 Technical Design Report* (CERN, Geneva, 2006), https://cds.cern.ch/record/1004186.

[30] B. L. Miller, D. E. Goldberg *et al.*, Genetic algorithms, tournament selection, and the effects of noise, Complex Syst. **9**, 193 (1995), https://content.wolfram.com/uploads/sites/13/2018/02/09-3-2.pdf.

[31] S. Dash, B. K. Tripathy *et al.*, *Handbook of Research on Modeling, Analysis, and Application of Nature-Inspired MetaHeuristic Algorithms* (IGI Global, Hershey, PA, 2017), 10.4018/978-1-5225-2857-9.

[32] M. Ferrario, Slater's theorem for magnetic mirror boundary perturbations, Part. Accel. **46**, 217 (1993), https://inspirehep.net/files/e5306984615b622a7ae4ca9ff8c22103.

[33] D. A. Swenson, E. A. Knapp, J. M. Potter, and E. J. Schneider, Stabilization of the drift tube linac by operation in the $\pi/2$ cavity mode, in *Proceedings of 6th International Conference on High Energy Accelerators, HEACC 1967, Cambridge, Massachusetts* (Cambridge Electron Accelerator, Cambridge, MA, 1967), pp. 167–173, https://inspirehep.net/files/fc4570a2a4c834f618c26814b6bda3aa.

[34] S. Machida, T. Kato, and S. Fukumoto, Stabilizing characteristics of post-couplers, IEEE Trans. Nucl. Sci. **32**, 3259 (1985).

[35] M. Vretenar and D. J. Warner, Field stabilization in the quasi-Alvarez structure, in *Proceedings of the Linear Accelerator Conference 1990, Albuquerque, NM* (JACoW, Geneva, Switzerland, 1990), pp. 96–98, https://accelconf.web.cern.ch/l90/papers/mo420.pdf.

[36] J. H. Billen, G. Spalek, and A. H. Shapiro, Field stability in two-stem drift-tube linacs, in *Proceedings of the 1988 Linear Accelerator Conference, Williamsburg, VI* (Continuous Electron Beam Accelerator Facility, Newport News, VI, 1988), pp. 125–127, https://accelconf.web.cern.ch/l88/papers/mo3-35.pdf.

[37] M. R. Khalvati and S. Ramberger, Tuning and field stabilization of the CERN Linac4 drift tube linac, in *Proceedings of the 27th International Linear Accelerator Conference, LINAC2014, Geneva, Switzerland* (JACoW, Geneva, Switzerland, 2014), pp. 631–633, https://accelconf.web.cern.ch/LINAC2014/papers/tupp089.pdf.

[38] T. P. Wangler, *RF Linear Accelerators* (John Wiley & Sons, New York, 2008), 10.1002/9783527623426.

[39] F. Grespan, Equivalent circuit for postcoupler stabilization in a drift tube linac, Phys. Rev. ST Accel. Beams **15**, 010101 (2012).

[40] F. Gerigk, Status and future strategy for advanced high power microwave sources for accelerators, in *Proceedings of 9th International Particle Accelerator Conference, IPAC'18, Vancouver, BC, Canada* (JACoW, Geneva, Switzerland, 2018), pp. 12–17, 10.18429/JACoW-IPAC2018-MOYGB1.

[41] J. Cai, I. Syratchev, and Z. Lui, Scaling procedures and post-optimization for the design of high-efficiency klystrons, IEEE Trans. Electron Devices **66**, 1075 (2018).